


Executive Summary Report Issue 1, Rev. 1	Ref Four-A-M/ESR/22001		Page 1 of 15





Advanced Aluminium Alloys tailored for
Additive Manufacturing space applications, targeting
high end structural spacecraft parts

(Four-A-M Project)

Executive Summary Report

Contract: 4000125120/18/NL/LvH

Written by:	N. Jimenez Mena (CRM)
	 Date: 28/10/2022
Released by:	N. Nutal (CRM)
	 Date: 28/10/2022

			
Executive Summary Report Issue 1, Rev. 1	Ref Four-A-M/ESR/22001		Page 2 of 15

Distribution List

Recipients	Affiliation	Nr. of Copies
Andrew Norman	ESTEC	1 copy
Nicolas Nutal	CRM	1 copy
Cédric Georges	CRM	1 copy
Norberto Jimenez Mena	CRM	1 copy
Brecht Van Hooreweder	KULeuven	1 copy
Ann Witvrouw	KULeuven	1 copy
Emilie Beevers	KULeuven	1 copy
Nele Moelans	KULeuven	1 copy
Daiman Zhu	KULeuven	1 copy
Lore Thijs	3DS	1 copy
Koen Huybrechts	3DS	1 copy
Nachiketa Ray	3DS	1 copy
Stéphane Lelij	SABCA	1 copy
Philippe Hendrickx	SABCA	1 copy

Document Change Record

Issue	Date	Modifications
1	18/10/2022	original





			
Executive Summary Report Issue 1, Rev. 1	Ref Four-A-M/ESR/22001		Page 3 of 15

Table of contents

<u>1.</u>	<u>Introduction.....</u>	<u>4</u>
<u>2.</u>	<u>Design and fast testing of new compositions (Phase A)</u>	<u>4</u>
	2.1.Thermodynamic modelling.....	4
	2.2.Fast solidification behaviour screening.....	5
<u>3.</u>	<u>Additive Manufacturing of selected alloy (Phase B)</u>	<u>8</u>
	3.1.Laser Powder Bed Fusion (LPBF) trials	8
	3.2.Laser Metal Deposition (LMD) trials	12
	3.3.Other observations.....	13
<u>4.</u>	<u>Conclusions of the project</u>	<u>14</u>

List of Abbreviations

AM	Additive Manufacturing
CALPHAD	CALculation of PHase Diagrams
DED	Direct Energy Deposition
EBM	Electron beam melting
EBW	Electron beam welding
ECSS	European Cooperation for Space Standardization
ESA	European Space Agency
ESTEC	European Space Research and Technology Centre
GSTP	General Support Technology Program
LPFB	Laser Powder Bed Fusion
LMD	Laser Metal Deposition
MSP	Melt spinning
RP	Rapid Prototyping
PSD	Particle Size Distribution
SEM	Scanning Electron Microscopy
SLM	Selective Laser Melting
SoW	Statement of Work
TBC	To Be Confirmed
TBD	To Be Defined
TN	Technical Note
WAAM	Wire Arc Additive Manufacturing
WLAM	Wire Laser Additive Manufacturing

			
Executive Summary Report Issue 1, Rev. 1	Ref Four-A-M/ESR/22001		Page 4 of 15

1. Introduction

Recently, additive manufacturing (AM) has been increasingly used for structural components in aerospace applications and military and civil aircrafts. There are two main reasons for this:

- Powder bed processes (LPBF or EBM) possess high degree of design freedom compared to conventional manufacturing methods;
- AM processes do not need tooling. Therefore, this leads to cost delivery time reduction for prototypes;

There are, however, some drawbacks:

- The design freedom is real for powder bed processes (even if there are shape limitations) but it is not the case for blown powder or wire + arc methods;
- The size is limited. This is less the case for blown powder or wire + arc methods;
- It is limited to alloys that are readily weldable (titanium and some aluminium alloys). Therefore, many families of aluminium alloys with high strength, toughness and/or damage tolerance, such as 2xxx or 7xxx series, are not compatible.

Due to the novelty and harsh conditions of the process with cooling rates ranging from 10^2 up to 10^6 K/s, new materials need to be developed, and by extension, adapted development routes that account for the process features. There are two elements main steps in the alloy development for AM: (i) new alloy development and (ii) compatibility with AM process. The classical route to test novel materials involves:

- Definition and casting of the alloy;
- Atomizing of the powder;
- Screening of the AM process parameters;
- Production of the samples by AM process(es).

This route is a rather expensive if several compositions want to be tested atomisation of the powder and optimisation of the AM process parameters is time consuming and expensive. In addition, this process must be performed for three different techniques showing large differences in cooling rates (i.e., LPBF, LMD and WAAM).



In this work an alternative route is explored:

- 1) Alloy design and microstructure modelling;
- 2) Fast screening and testing of alloys at solidification rates close to those observed in AM processes via rapid solidification techniques;
- 3) Atomization of selected alloy;
- 4) Testing of the selected alloys in AM process.

2. Design and fast testing of new compositions (Phase A)

2.1. Thermodynamic modelling

The newly developed alloy is based on 7xxx series, i.e., containing Zn and Mg as main alloying elements. It provides high strength and toughness and it already used in aerospace applications. The strategy to reduce the tendency to hot cracking is based on grain refinement of the solidifying microstructure. To do so, transition elements known to provide grain refinement via primary

			
Executive Summary Report Issue 1, Rev. 1	Ref Four-A-M/ESR/22001		Page 5 of 15

precipitation have been studied. These will be referred to as “grain refining” elements in the present document.

Within this framework, the effect on the microstructure and solidification behaviour of different elements and concentrations were studied using the CALPHAD approach. In particular, this methodology allowed determine the type and amount of phases to be formed during the solidification process. Scheil calculations based on equilibrium diagrams as shown in Figure 1-left provide an example of this for an alloy containing 1% of grain refining elements.

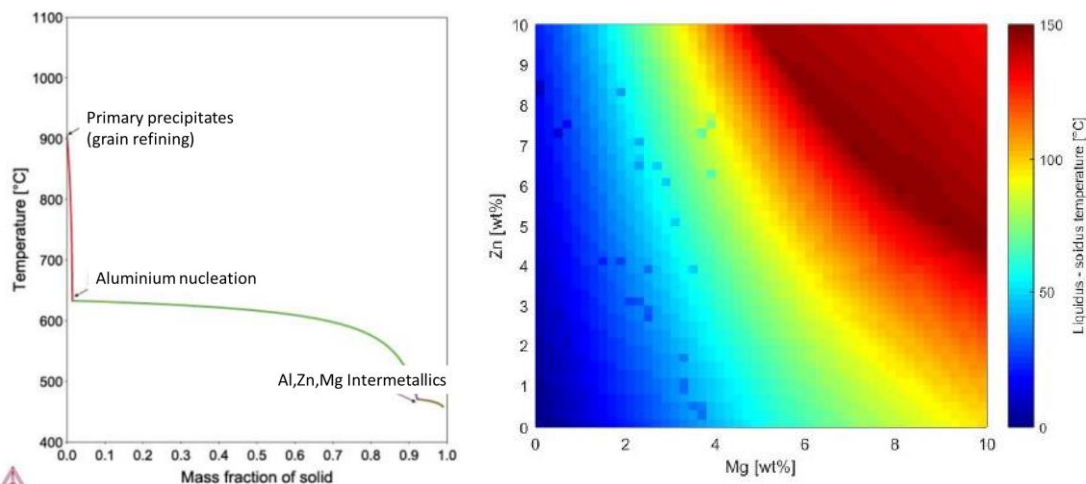


Figure 1: (left) Scheil-calculated solidification path for one of the candidate aluminum alloys containing grain-refining elements. (right) liquidus-solidus temperature range as a function of the Zn and Mg content to predict the initial hot cracking susceptibility.

The cracking susceptibility of the alloys was also limited based on the liquidus-solidus temperature range as mapped in Figure 1 as a function of the Zn and Mg concentrations. The selection of the alloy avoided the red regions in the diagram.

This thermodynamic study allowed to fix one composition regarding the Zn and Mg elements and select several grain-refining element concentrations and combinations. For the sake of the intellectual property protection, the actual compositions are not disclosed in this document.

2.2. Fast solidification behaviour screening

The alloys selected from thermodynamic modelling underwent fast solidification techniques to assess their compatibility with AM processes. Two techniques were used: (i) melt spinning (MSP) and (ii) electron beam welding (EBW). For calibration purposes both techniques were first performed with commercial AA2024 and compared to LPBF AA2024. A comparison of the achieved cooling rates is provided in Figure 2.

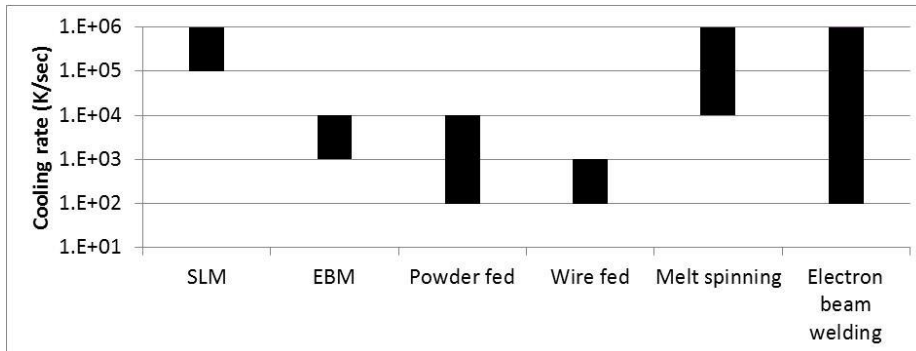


Figure 2: Achieved cooling rates for selected fast cooling methods, compared to classical additive manufacturing processes.

The **melt spinning** method consists of the pouring of a melt onto a spinning copper wheel that quickly cools down the aluminium creating a continuous ribbon. An example of the ribbon and the cross section are provided in Figure 3. The cross section indicates the estimated cooling rates at different sections of the ribbon's thickness.



Figure 3: (left) view of a melt spun ribbon (right) cross section of the melt spun ribbon after etching. The solidification rates included in the picture are estimated from the size of the microstructure at different regions of the thickness.

The pictures in Figure 4 show the Electron Back-Scattered Diffraction maps of MSP'ed selected alloys. It can be observed that only some selected grain refining elements do provide a transition from columnar to small equiaxed, which is the goal. However, this method does not provide information on the solidification cracking susceptibility of the alloys.

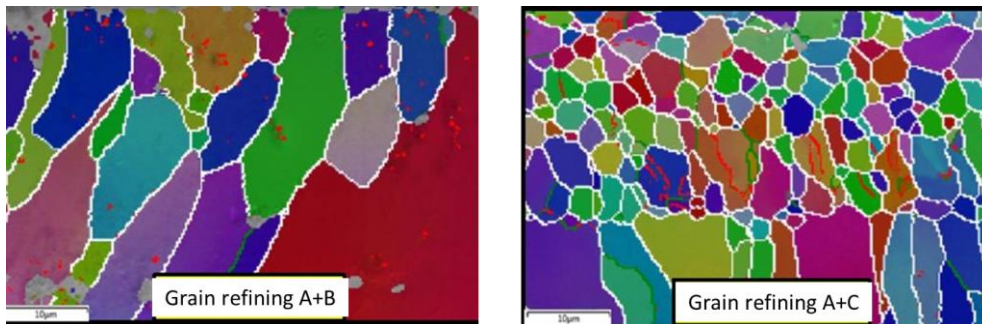


Figure 4: EBSD orientation maps showing (left) the columnar microstructure for a composition where the grain refinement effect is not activated and (right) a microstructure in which there is a refinement and a columnar-to-equiaxed transition.

The **Electron Beam Welding** method consists of performing a fast welds bead using an electron beam in a vacuum chamber. Scanning speeds of the beam range from those of LMD to those of LPBF. The welded bead is carried out on casted ingots as shown in Figure 5-left. An example of the cross section of a EBW'ed specimen showing some cracking is provided in Figure 5-right.

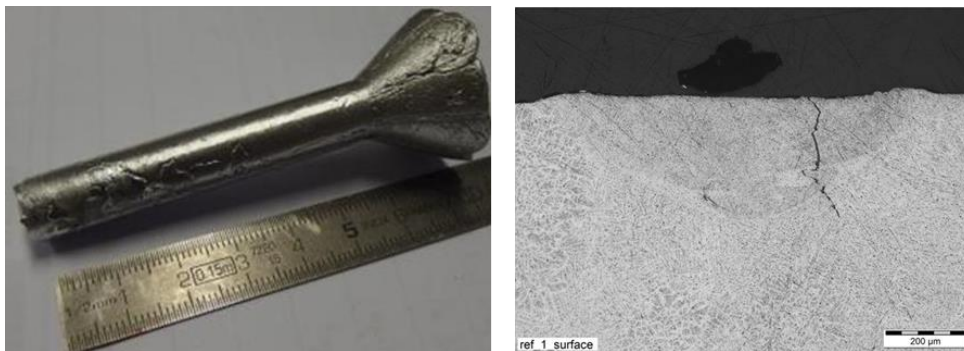


Figure 5: (left) View of a cast ingot used for EBW trials and (right) cross section of the molten pool in an EBW'ed ingot showing a solidification crack.

To complete the selection of the alloys, the age hardening of the alloys was also measured. Nano-indentation was performed on MSP ribbons after thermal treatment to assess the hardness.

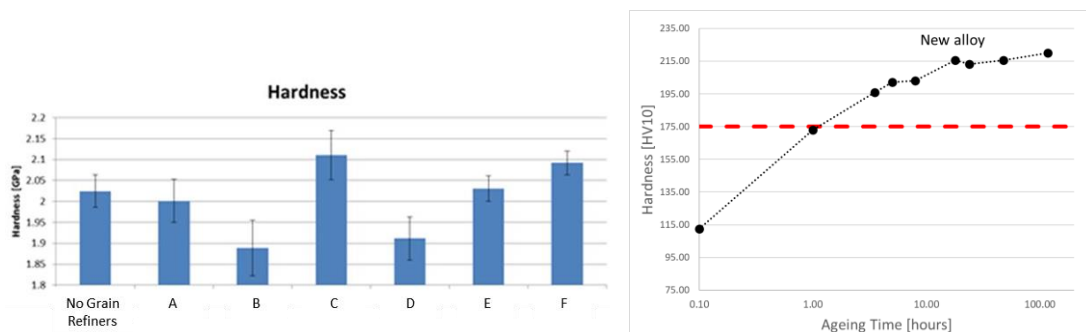


Figure 6: (left) nano-hardness measured in the ribbons after solutioning treatment for different grain-refiner combinations and concentrations. (right) Evolution of the hardness of the selected alloy for phase B as a function of age treatment duration. The red line indicated the hardness of a wrought AA7075-T6 alloy.

The results provided in Figure 6-left along with the cracking resistance measured with EBW and grain refining potential revealed by MSP allowed for the selection of one alloy to be atomised and tested in LPBF and LMD conditions. The optimised thermal treatment for this alloy was also developed. The hardness as a function of age-hardening time, after solutioning and quenching, is provided in Figure 6-right. The achieved hardness is well over 200HV, which is over the reference value for AA7075 (175 HV).

3. Additive Manufacturing of selected alloy (Phase B)

The selected alloy was tested in two additive manufacturing conditions: (i) LPBF showing the harshest cooling conditions and (ii) LMD with slower cooling rates. In both cases, the first step was to perform a parameter optimization. Selected parameters providing the best density were kept printing specimens for mechanical characterization. Mechanical characterization was performed on the as-built and T6 temper states and compared to the literature.

3.1. Laser Powder Bed Fusion (LPBF) trials

The main work on the optimisation side was performed by changing the laser power, scanning speed and laser spot diameter. The optimisation was carried on small cubes. It was possible to find a parameter window for each of the laser spot diameters in which the microstructure and Archimedes density measurements revealed a good health of the materials (few pores, free of cracks). An example of the parameter optimization for the larger spot size is provided in Figure 7. Cells highlighted in dark green show the optimised parameter region.

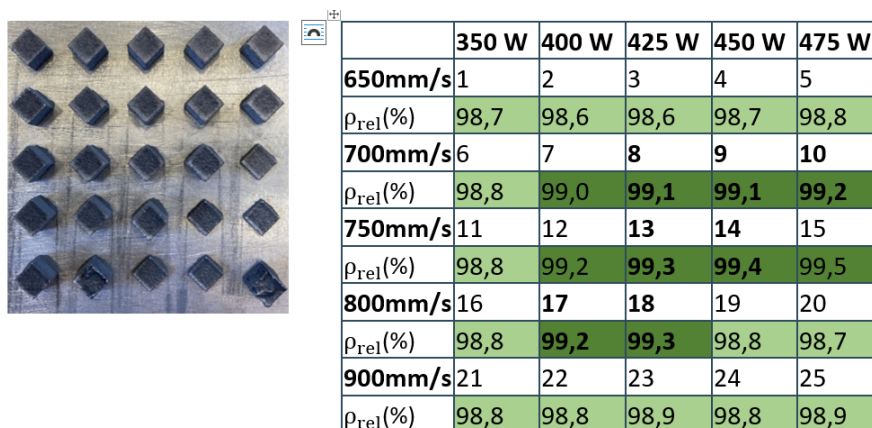






Figure 7: Optimization study performed on cubes for the selected alloy. For these tests the laser spot size was the larger one (80 vs 50 μm diameter). The dark green cells indicate the parameters were Archimedes testing revealed a density over 99%.

Some examples of the optimised parameters for both laser spot sizes are provided in Figure 8. In general, a larger spot showed better density results and a better finishing on the upper surface of the printed cube.

			
Executive Summary Report Issue 1, Rev. 1	Ref Four-A-M/ESR/22001		Page 9 of 15

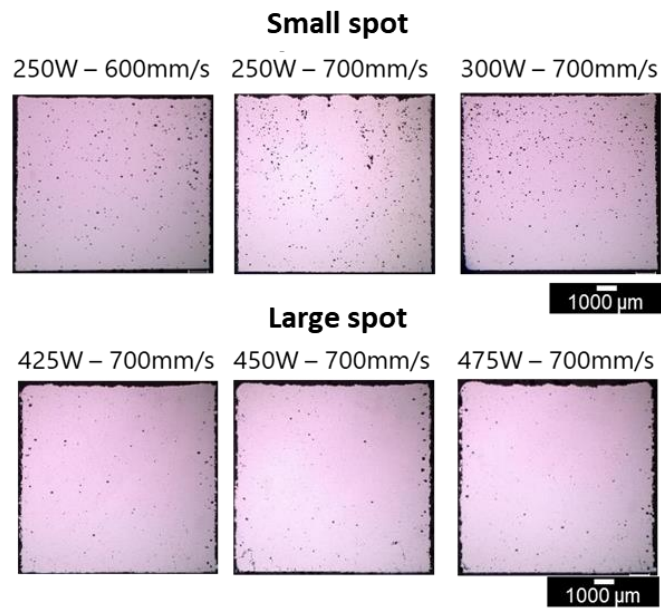


Figure 8: Comparison of the optimized parameters for the selected alloy using two different laser spot diameters: (Top) Small laser spot size, 50 μm, and (bottom) large spot size, 80 μm. The effect of the preheating the building plate was also studied. It can be seen that, as the temperature increases in the building plate, the formation of defects does also change (Figure 9-left). They go from solidification cracks at the beginning of the print (when the system is at room temperature), to some irregular porosity identified as keyhole at the top of the print (when the temperature is ~200 °C).

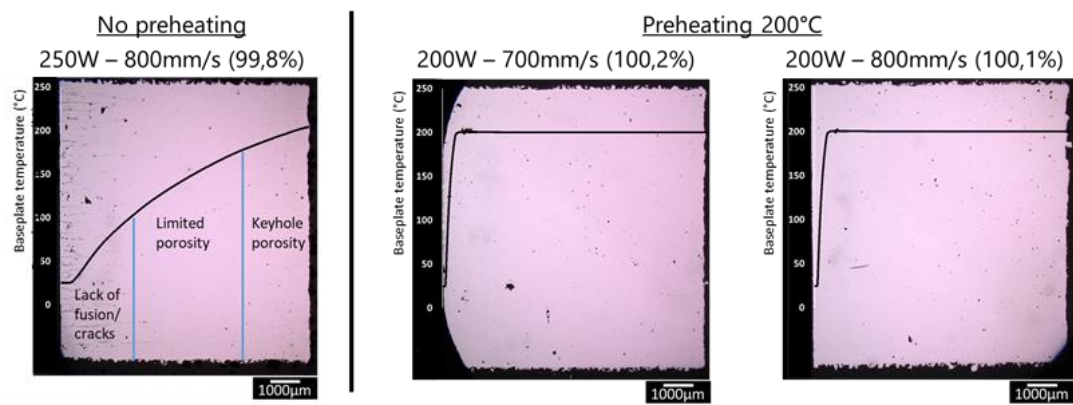



Figure 9: Effect of the build plate temperature on the formation of defects. (left) no preheating is used, there is an evolution of the temperature showing solidification cracking in the early stages and increasing porosity as the temperature increased. (left) tests with preheating of the baseplate at 200 °C. The amount of defects (both cracks and porosity) are lower that in the no-preheating case.

Once the parameters were chosen, a breadboard with characterization specimens was printed. It has to be noted that this breadboard was printed without preheating since it is not a commercially available solution and the optimization without preheating already provided good results. The

			
Executive Summary Report Issue 1, Rev. 1	Ref Four-A-M/ESR/22001		Page 10 of 15

printed breadboards are shown in Figure 10. It can be observed that the surface aspect is quite rough and blackened.

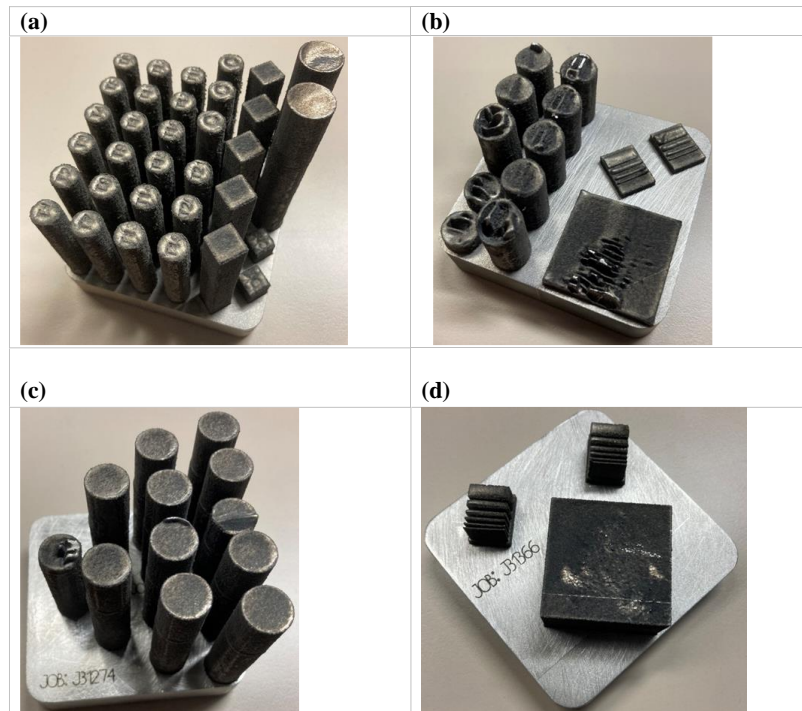


Figure 10: Breadboard printing with the optimized parameters. Larger prints were not successful as it can be observed from the blackened surfaces and the uneven top surfaces of some of the specimens.

Prior to testing, the cross section of some of the specimens was observed. Some examples are provided in Figure 11. It can be seen that, within the same specimen, the defect types and volume change significantly. From general porosity that accumulates close to the lateral surface of the specimen to solidification cracks that propagate from the core. The extensive porosity has been related to the overheating in the chamber during the process. The cracks, on the other hand, are related to a drop of temperature in the system and higher cooling rates.

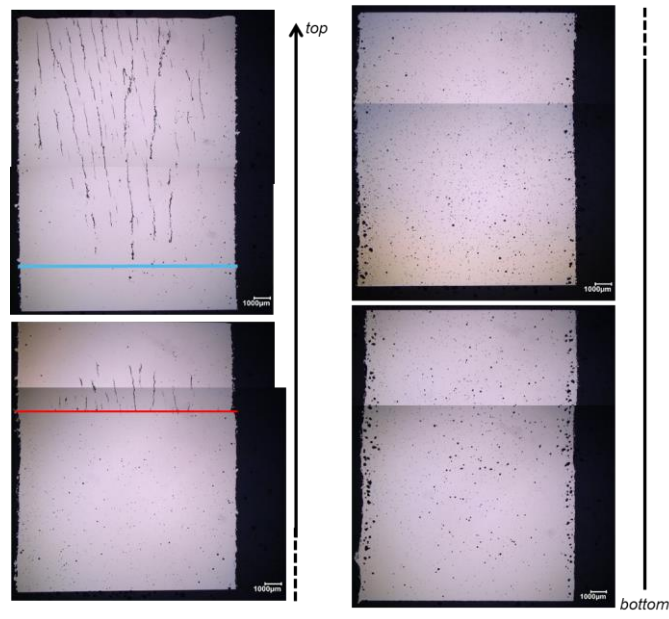
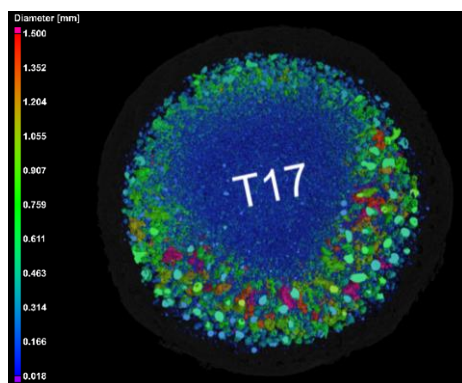


Figure 11: Cross section of one of the tallest breadboard samples showing the presence of several defects such as porosity (accumulated below the surfaces) and solidification cracks




X-ray CT scan in Figure 12-left confirms the accumulation of porosity volume fraction at the contour of the specimen. It also revealed that, by machining, most of the porosity will be removed and tensile specimens could be tested. The results in the “As-built” and “T6” temper states are summarized in on Figure 12-right. Reference values for other aluminium alloys processed by LPBF are also included for comparison.



Alloy (temper)	Yield Strength [MPa]	Tensile Strength [MPa]	Elongation [%]
4AM alloy (as-built)	201 ± 2	251 ± 3	10 ± 1
4AM alloy (T6)	425 ± 5.6	442 ± 4	5 ± 2
A205 (heat treated)	370 - 430	460 - 510	-
Scalmalloy (heat treated)	490 ± 15	520 ± 15	16 ± 3

Figure 12: (left) X-ray CT scan showing the accumulation of porosity closer to the contour of the specimen. (right) tensile results for the new alloy processed by LPBF in the as-built and T6 states, both in the vertical direction. The table includes values for the commercial Al alloys A205 and Scalmalloy

The origin of the defects and the different results when upscaling the prints are not fully understood. Two phenomena can be the origin of such porosity. The contour of the samples is the zone where the printed part reaches the highest temperatures during the processing, thus, the origin of porosities is somewhat related to the reached temperature of that region. High concentration of Zn is known to promote the formation of a keyhole that can bring the so-called keyhole porosity. On the

			
Executive Summary Report Issue 1, Rev. 1	Ref Four-A-M/ESR/22001		Page 12 of 15

other hand, gas porosity brought by the precipitations of dissolved hydrogen is known to be related to the solidification rates. The heat dissipation in the contour is lower than in the core, thus, the pores have more time to nucleate and grow. In both cases, a control of the power and temperature during printing should improve the health of the samples.

3.2. Laser Metal Deposition (LMD) trials

In parallel, a similar work as performed for LPBF was performed for Laser Metal Deposition (LMD). In this case, the higher size fraction of the powder was used for printing (+45/-105 μm). The parametrization was performed on small printed volumes. On these volumes an optical measurement of the density was carried out. For most of the parameters, the density was over 99.5%.

Figure 13 shows an example of the cross section of one of the tested parameters. In this case the porosity is $\sim 0.2\%$. The EBSD map on the left-hand side of the figure shows a transition from the substrates (AA5083) to the newly developed aluminium alloy. The first deposited layer shows still a columnar microstructure due to a dilution of the composition with the substrate. At the third layer, the equiaxed microstructure is fully developed.

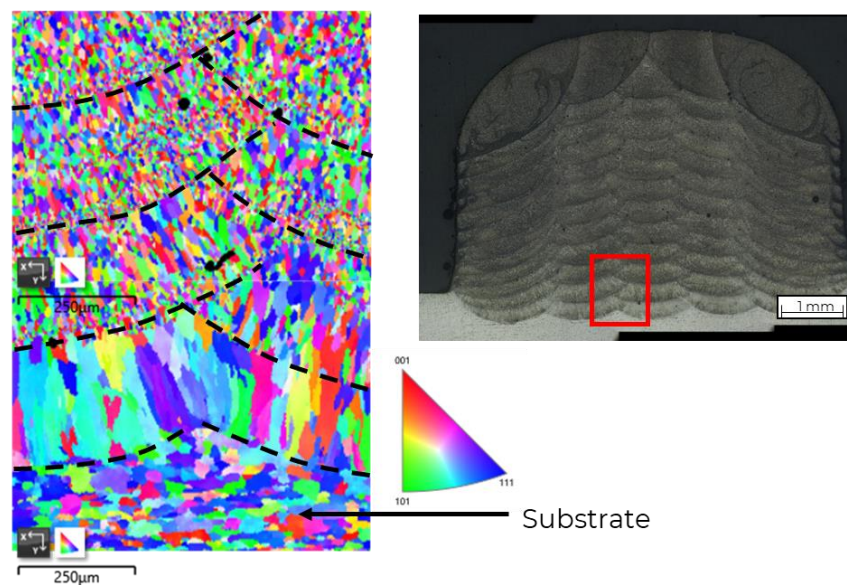


Figure 13: (right) Macro-optical observation of the cross section of the “cold” specimen after etching. (Left) EBSD orientation map performed on the region delimited by the red square in the right figure showing the transition between the substrate and the print in the first layers.

A set of parameters was selected to print a coupon for mechanical characterization. The coupon is shown in Figure 14-left. From this coupon, metallographic, heat treatment and tensile experiments were performed. The cross section of the wall is also provided in Figure 14-right. The porosity for this coupon was measured to be below 0.1%.

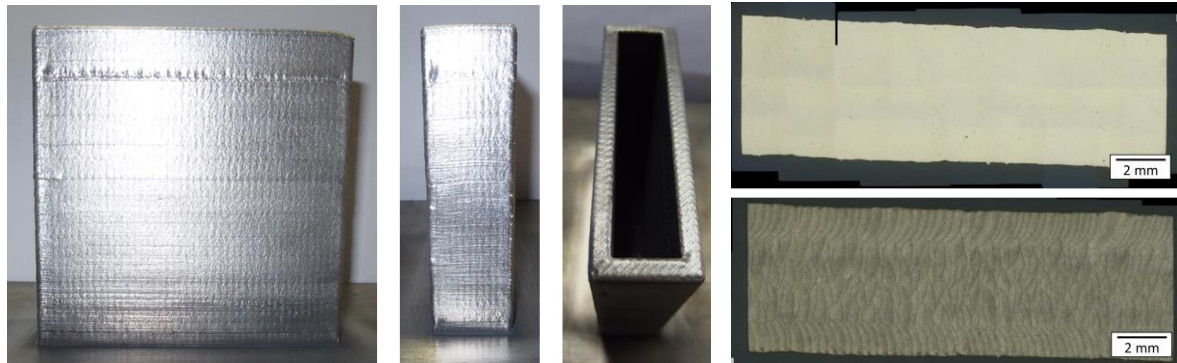
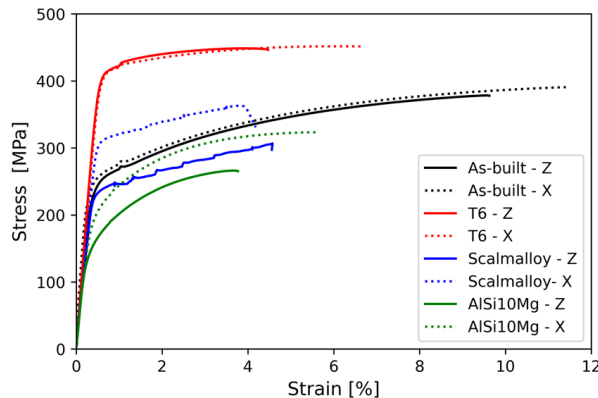


Figure 14: (left) View of the LMD printed coupon (right) cross section observations before and after etching showing a porosity below 0.1%.

Tensile samples were cut and tested in two directions, parallel to the substrate (X-direction) and perpendicular to the substrate (Z-direction). Two temper states were tested: As-built and T6. Figure 15 shows an example of tensile curves for this alloy (black and red lines) compared to two other alloys also processed by LMD (Scalmalloy and Al10SiMg). The results show that this new alloy does not show any anisotropy due to the equiaxed microstructure, contrary to the commercial solutions. The yield strength in the as-built state is already higher than those observed for Al10SiMg and Scalmalloy. In the T6 state, the yield strength is over 400 MPa.



Specimen (Z direction)	R _{p0,2} [MPa]	R _m [MPa]	A [%]
As-built	250	370	7,0
T6	400	450	4,0
Scalmalloy (Aged, LMD @ CRM)	235	308	5,9
AlSi10Mg (Aged, LMD @ CRM)	153	263	3,1

Figure 15: (left) Flow curves for the new alloy and comparison with other commercial alloys processed by LMD. (right) comparison of the tensile stress results in the Z-direction for the selected alloy in two tempers and Al10SiMg and Scalmalloy commercial solutions.

3.3. Other observations

It is worth noting that Zn and Mg evaporation was observed in both process. Table 1 shows the percentage of Zn and Mg evaporated from the initial powder for two power intensities in LMD (high and low), and LPBF. The evaporation of Zn and Mg results in a lowering of the mechanical properties since the amount of precipitates is reduced. In future work, the initial powder should have an additional concentration in Zn and Mg to compensate for their evaporation during processing.

Sample	Zn (% loss)	Mg (% loss)
LMD coupon (high laser power)	49	20
LMD coupon (low laser power)	34	8
LPBF Coupon	27	9

Table 1: Zn and Mg evaporation after printing for LMD and LPBF processing techniques.

The effect of this evaporation can be observed in the age-hardening curves for the reference cast alloy and the processed coupons (Figure 16). The hardening curves for LPBF and LMD are similar. The loss of alloying elements results in a drop of hardness for LPBF and LMD compared to the cast reference. It is expected that, in the right conditions of composition, the alloy will provide a hardness for both processes as good as the one observed for wrought AA7075-T6.

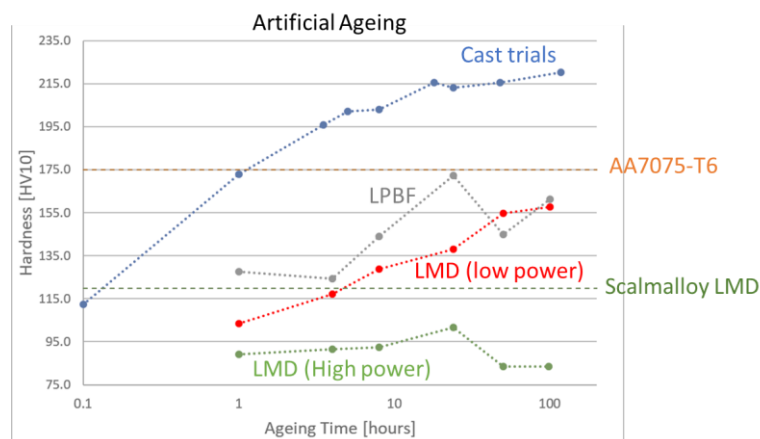






Figure 16: Evolution of the hardness as a function of the duration of the age hardening treatment for the novel alloy processed by cast, LMD and LPBF.

4. Conclusions of the project

- A new high strength aluminium alloy has been developed using a modelling + experimental approach;
- The CALPHAD method was used to select some candidate alloys where the grain refining effects were predicted;
- A novel methodology for fast screening the behaviour of alloys in additive manufacturing conditions was developed. By combining melt spinning, casting and electron beam welding it was possible to classify and select the best alloy in terms of microstructure, hot cracking resistance and hardness;
- The selected alloy was tested in additive manufacturing conditions:
 - For LPBF, reduced size trials showed the presence of a narrow optimal range for printing. Using preheating and a larger laser spot size, the density increases. The optimized parameters did not show solidification cracking but the productivity is lower than the optimum parameters observed for other Al alloys;

			
Executive Summary Report Issue 1, Rev. 1	Ref Four-A-M/ESR/22001		Page 15 of 15

- For larger LPBF prints, an accumulation of heat was observed that led to high porosity in the specimens.;
- For LMD, the optimized parameter window is larger and the porosity below 0.5%. No additional porosity is brought when printing larger parts;
- The heat treatment of the alloy was optimized and the mechanical results show yield strengths >400 MPa, elongation ~5% and no anisotropy;
- Evaporation of Zn was intensive for both processes. An initial compensation of the Zn loss should be included in the initial powder. Higher strengths are thus expected for a more refined composition.